# Structure of the nucleotide-binding domain of *Plasmodium falciparum* Rab6 in the GDP-bound form

**Debasish Chattopadhyay,[a,b]
Gordon Langsley,[c] Mike Carson,[b]
Rosario Recacha,[b] Lawrence
DeLucas[b] and Craig Smith[b]***

[a]Division of Geographic Medicine, University of Alabama at Birmingham, AL-35294, USA, [b]Center for Macromolecular Crystallography, University of Alabama at Birmingham, AL-35294, USA, and [c]Laboratoire de Signalisation Immunoparasitaire, URA CNRS 1960, Department of Immunology, Pasteur Institute, Paris, France

Correspondence e-mail: smith@cmc.uab.edu

Rab proteins are small Ras-like GTPases which play important roles in regulating intracellular vesicle trafficking. The nucleotide-binding domain of Rab6 from the malaria parasite *Plasmodium falciparum* was crystallized with GDP bound to the active site. The MAD phasing technique was used to determine the crystal structure to 2.3 Å resolution. Comparisons of the structure of GDP-bound *Pf*Rab6 with the recently determined structures of Rab3A in complex with either a GTP analog or with GTP and Rabphillin present structural evidence supporting the traditional model for the molecular GTP/GDP switch in Rab proteins. *Pf*Rab6 residues homologous to those distinguishing human Rab6 isoforms, which differ in binding to Rabkinesin-6 in human cells, are located next to the recognized complementarity-determining region (CDR) and constitute a conceptual broadening of that domain. Despite significant observable differences in Golgi ultrastructure, the Rab6 core structure and switch mechanism appear highly conserved when compared with murine Rab3a structures. A significant difference between the *Pf*Rab6 and higher eukaryotic Rabs may be the lack of CDR features that allow binding interactions with Rabkinesin-type effectors.

## 1. Introduction

Proteins and lipids in eukaryotic cells are carried between intracellular compartments by way of exocytic and endocytic pathways. Carrier vesicles bud from donor organelles and are targeted to the appropriate acceptor organelles to which the vesicles fuse through recognition of specific receptors (Pfeffer, 1994). A variety of GTPases alternate between conformational states *via* nucleotide exchange and GTP hydrolysis and act as molecular switches. They play critical roles in the sorting and transport of proteins and other molecules among subcellular compartments and to the extracellular membrane (Nuoffer & Balch, 1994; Kjeldgaard *et al.*, 1996; Sprang, 1997). Two areas, referred to as switch I and switch II in the structure of GTPases, undergo conformational changes owing to GTP hydrolysis. This switch signal is communicated in an organized and sequential manner throughout the trafficking pathway by way of specific protein–protein interactions involving GTPases and various other components referred to as effector molecules. They also possess variable sequences called complementarity-determining regions (CDR) outside the nucleotide-binding motifs that specify signatures for a particular function and determine targeted interactions with the other proteins (Kjeldgaard *et al.*, 1996).

The Rab proteins are a large family of monomeric Ras-related GTPases (Pfeffer, 1994; Martinez & Goud, 1998).

Rabs attach to the surface of distinct membrane-bound organelles and mediate the v-SNARE (vesicle-soluble $N$-ethyl maleimide-sensitive factor-attachment protein receptor) and t-SNARE (target-SNARE) recognition processes by which transport vesicles dock with their cognate target membranes. The Rabs then bind to Rab-specific GAPs (GTPase activating proteins), which enhance the hydrolysis of GTP to GDP. A cytosolic protein, GDP dissociation inhibitor (GDI), retrieves GDP-bound Rab proteins from cellular membranes. Guanine nucleotide-exchange factor (GEF) bound to the donor membrane cytosolic surface dissociates GDI from the Rab and causes the exchange of GDP for GTP. The Rab–GTP then becomes membrane-bound to a new transport vesicle in association with another v-SNARE on its way to the target membrane to complete the cycle (Pfeffer, 1994; Schimmöller et al., 1998).

Rab6 is found in eukaryotes and mammalian cells on the cytosolic side of medial and trans cisternae of the Golgi apparatus and the membranes of the trans Golgi network (TGN; Goud et al., 1990; Antony et al., 1992). It appears to be involved with retrograde vesicle transport between the Golgi and the endoplasmic reticulum (ER) and mediates the recycling of Golgi enzymes through the ER, particularly those involved in glycosylation (Martinez & Goud, 1998; Girod et al., 1999). Both the force and the direction of transport are believed to be generated through its interaction with the Rabkinesin-6 molecular motor (Echard et al., 1998).

P. falciparum is the most lethal strain of the obligate intracellular parasite that causes human malaria. P. falciparum is different from mammalian cells but similar to Saccharomyces cerevisiae in that it has a rudimentary Golgi apparatus consisting of a single cisternum with no apparent TGN. In spite of this simple Golgi structure, both S. cerevisiae and P. falciparum encode unique rab6 genes, viz. ypt6 and Pfrab6, respectively (Strom et al., 1993; de Castro et al., 1996; Templeton & Kaslow, 1998). The absence of stacked Golgi cisternae has been linked to the lack of $N$-glycosylation in malaria parasites (Ward et al., 1997). Owing to the structural simplicity of the Golgi, it would appear that Rab6 in these lower eukaryotes cannot mediate retrograde transport from a non-existent TGN/Golgi cisternae stack to the ER and it is plausible that it performs some other ancestral function.

In order to gain insights into the possible function of PfRab6, we have determined its crystal structure using the multiwavelength anomalous dispersion (MAD) phasing technique. We found variant residues which distinguish newly identified human Rab6 isoforms (Fitzgerald & Reed, 1999) located next to the PfRab6 RabCDR region. This constitutes a broadening of the CDR region as identified in the structure of murine Rab3A–GTP complexed with Rabphillin (Ostermeier & Brunger, 1999). Importantly, comparison of GDP-bound PfRab6 to the recently determined structures of Rab3A in complex with a GTP analog (Dumas et al., 1999) and in complex with GTP and Rabphillin (Ostermeier & Brunger, 1999) confirms the general model for the molecular GTP/GDP switch in Rab proteins.

## 2. Materials and methods

### 2.1. Expression and purification

Methods describing the expression and purification of wild-type PfRab6t have been described elsewhere (Chattopadhyay et al., 2000). The coding sequence for P. falciparum Rab6 residues 1–175 was PCR amplified and engineered into the NcoI and HindIII sites of Escherichia coli expression vector pET21a (Novagen Inc.). The recombinant protein was induced in E. coli BL21(DE3)pLysS cells by adding 1 mM isopropyl-$\beta$-D-thiogalactoside to the culture. The selenomethionine Rab6t was expressed in E. coli strain B834 pLysS by growing the culture in a selective medium containing all L-amino acids except methionine, which was substituted with L-selenomethionine (Sigma, USA).

The frozen bacterial pellet from 4 l of culture was lysed in 50 ml of buffer A (50 mM Tris acetate pH 8.2, 10 mM MgCl$_2$, 0.1 mM PMSF, 2 mM DTT) containing DNAase I (Sigma, USA) and was stirred for 30 min at 277 K. The lysate was subjected to centrifugation (35 000 rev min$^{-1}$ for 30 min). The supernatant was applied to a Q-Sepharose FF column (Pharmacia, 25 ml bed volume) pre-equilibrated with buffer A. The column was then washed with 125 ml of buffer A. The protein of interest was obtained in the column flowthrough and wash solution as revealed by SDS–PAGE. Solid ammonium sulfate was added to the pooled flowthrough and wash solution to attain 40% saturation. The suspension was subjected to centrifugation (30 000 rev min$^{-1}$ for 20 min) and the supernatant was brought to 70% ammonium sulfate saturation. The precipitate collected by centrifugation of the 40–70% ammonium sulfate saturation step contained the recombinant protein. The pellet was resuspended in 9 ml buffer B (20 mM Tris borate pH 9.25, 10 mM MgCl$_2$, 2 mM DTT) and dialyzed thoroughly against the same buffer. The dialyzate was applied to a MonoQ 10/10 (Pharmacia) column equilibrated with buffer B. After washing the column with ten column volumes of buffer B, the bound protein was eluted with a linear gradient of 0–400 mM NaCl in 15 column volumes of buffer B. 5 ml fractions were collected and analyzed by SDS–PAGE. Fractions containing selenomethionine PfRab6t eluted at approximately 200 mM NaCl concentration. The protein was nearly homogeneous as judged by SDS–PAGE. The purified protein was analyzed by mass spectrometry and compared with the mass spectrum of the wild-type PfRab6t to ascertain the incorporation of selenomethionine.

### 2.2. Crystallization and data collection

Crystals of PfRab6t were grown by vapor diffusion in hanging drops. Crystals of the wild-type protein (without selenomethionine substitutions) were routinely grown by mixing equal volumes of protein solution and a reservoir solution that contained 1.0 M sodium sulfate, 0.1 M sodium cacodylate pH 6.5. Crystals of the selenomethionine PfRab6t grown under these conditions were too small for X-ray diffraction experiments. Crystals of the selenomethionine-substituted protein were grown by mixing 4 µl of a reservoir solution containing 30% polyethylene glycol 8000, 0.3 M

**Table 1**
Refinement statistics.

| | |
|---|---|
| MAD phasing at 2.6 Å | |
| No. of Se total/found | 4/3 |
| Mean FOM from *SOLVE* | 0.55 |
| Mean FOM from *DM* | 0.75 |
| Structure refinement | |
| Resolution (Å) | 9.94–2.3 |
| No. of reflections, $F > 3\sigma$ | 13776 |
| $R/R_{free}$ (%) | 21.4/24.6 |
| No. of atoms | 1340 |
| Water molecules | 63 |
| *B* factors | |
| Protein | 35.6 |
| GDP and Mg | 31.9 |
| Water | 40.0 |
| Model r.m.s. deviations from ideality | |
| Bonds (Å) | 0.006 |
| Angles (°) | 1.20 |
| Dihedrals (°) | 23.30 |

ammonium sulfate, 0.1 *M* sodium cacodylate at pH 6.5 with 4 µl of protein solution. The mixture was equilibrated against 1 ml of reservoir solution at room temperature. Crystals of approximate dimensions $0.1 \times 0.1 \times 0.08$ mm grew in about a week. The rate of success of growing these crystals was also considerably lower than for the crystals of the wild-type protein.

Diffraction data were collected at the IMCA undulator beamline 19-A at the Advanced Photon Source synchrotron, Argonne National Laboratory, Illinios. The detector used was a MAR Research CCD. The crystal was cryopreserved in 30% glycerol and flash-cooled to 100 K in an $N_2$-gas Cryostream
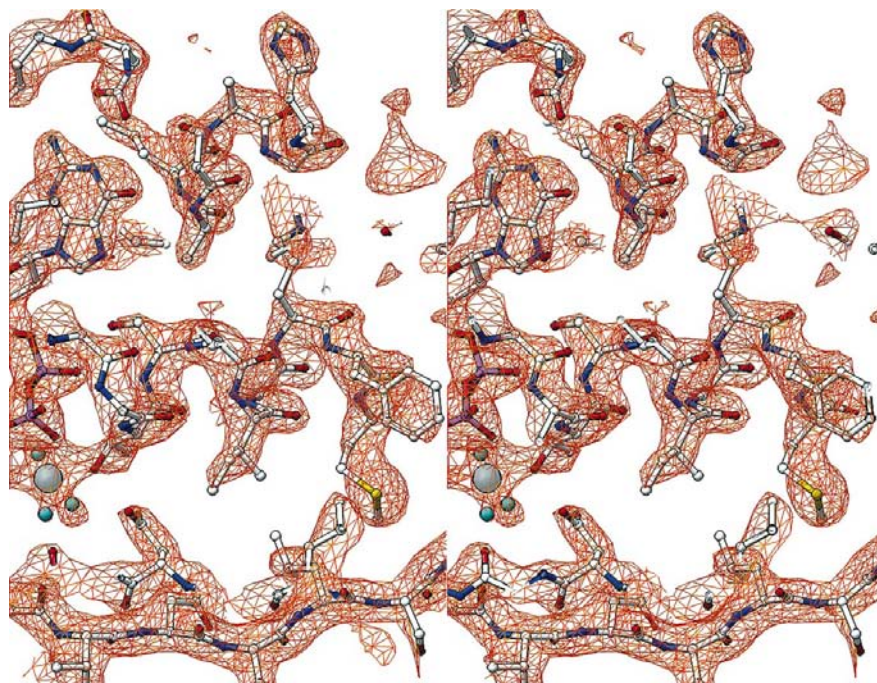
and diffracted to 2.2 Å resolution. Multiple-wavelength anomalous dispersion (MAD) data were collected from a single crystal at three wavelengths chosen on the basis of X-ray fluorescence measurements from the selenomethionine-containing crystal. The wavelengths used were 0.9789, 0.9770 and 0.9791 Å. 30° of oscillation data at a time were collected at each wavelength for 0.5° per frame and 60 s per frame. The crystal was then rotated by 180° and another 30° were collected the same way for each wavelength. Continuing with this procedure, 300° of contiguous oscillation data were collected at three wavelengths for the single crystal. The data were processed and scaled using *d\*TREK* version 4.1 (Molecular Structure Corporation, The Woodlands, Texas; Pflugrath, 1999). MAD data statistics are shown in Table 2.

### 2.3. Phasing and refinement

Experimental phases were determined to 2.3 Å resolution using the program *SOLVE* version 1.15 (Terwilliger & Berendzen, 1999). *SOLVE* found and refined three of the four Se positions. The fourth Se atom was in the disordered region of the molecule and was not visible in the resulting electron-density maps. The solvent-flattening program *DM* with skeletonization (Collaborative Computational Project, Number 4, 1994) was used to significantly improve the phases. The *CCP*4 program *FFT* was used to calculate the Fourier maps to 2.3 Å resolution and *QUANTA* (Molecular Simulations Inc., Burlington, Massachusetts) was used to display these very clean initial electron-density maps. Initial model building resulted in almost a complete tracing of the backbone structure. A theoretical model of the Rab6t structure based on a consensus model built from several small GTPase structures was produced using the program *MODELLER* (Sali & Blundell, 1993). This model was manually fitted to the observed $C^\alpha$ core structure. Manual changes to this structure were required to improve the main-chain and side-chain fit to the experimental electron density. Phe48 had electron density for two equally occupied positions that lay across a twofold crystal symmetry axis. This residue was fixed in one position for refinement and PDB deposition. Refinement statistics are shown in Table 1.

Structure refinement was performed with *CNS* version 0.9 (Brunger *et al.*, 1998) using 10% of the diffraction data randomly chosen for cross validation. Resolution cutoffs of the refinement procedure were 9.94 and 2.30 Å. Bulk-solvent modeling used the flat-model method with KSOL = 0.37 and BSOL = 34.41 Å$^2$. The $\sigma F$ cutoff for the data used was $3.0\sigma$.

The program *TOP* (Lu, 1996) was used to superimpose *Pf*Rab6t with other



**Figure 1**
MAD electron-density map. The map computed with experimental MAD phases is shown in stereo contoured at $2.0\sigma$. The refined atomic model is shown with the GDP at the left; the silver sphere is $Mg^{2+}$ and the cyan spheres are coordinated water molecules. All figures were prepared with *RIBBONS* (Carson, 1997), http://www.cmc.uab.edu/ribbons.

**Table 2**
Data collection.

*Pf*Rab6t MAD data statistics. Resolution was 19.82–2.20 Å for all wavelengths.

|  | Peak | Inflection | Remote |
|---|---|---|---|
| Wavelength (Å) | 0.9789 | 0.9791 | 0.9770 |
| $f'/f''$ | −6.8/+5.8 | −9.9/+2.2 | −5.0/+3.5 |
| Unit-cell parameters |  |  |  |
| $a$ (Å) | 81.20 | 81.16 | 81.30 |
| $c$ (Å) | 90.84 | 90.82 | 90.89 |
| No. of observed reflections | 294170 | 280299 | 293308 |
| No. of unique reflections | 15971 | 15956 | 16026 |
| Highest resolution shell (Å) | 2.28–2.20 | 2.28–2.20 | 2.28–2.20 |
| $R_{sym}$ overall/outer shell (%) | 8.7/31.8 | 8.7/32.8 | 8.2/34.0 |
| $I/\sigma$ overall/outer shell | 25.4/11.2 | 24.3/10.5 | 24.1/10.0 |
| Completeness (%) | 100 | 100 | 100 |
| Redundancy | 18.4 | 17.6 | 18.3 |

GTPase structure for three-dimensional alignment and to quantify structural differences.

## 3. Results

The recombinant construct of *P. falciparum* Rab6 (a C-terminally truncated version designated here as *Pf*Rab6t) containing the coding sequence for the catalytic domain (residues 1–175) was expressed in *E. coli*. Crystals were prepared using the GDP-bound protein. These crystals belong to the tetragonal space group $P4_32_12$, with unit-cell parameters $a = b = 81.2$, $c = 90.8$ Å. The crystal structure of the *Pf*Rab6t construct was determined using a selenomethioine-substituted form of the protein. Crystals of the selenomethionine *Pf*Rab6t grew under conditions similar to that of the wild-type protein. Mass-spectrometric analysis of the purified protein confirmed that all four methionine residues in *Pf*Rab6t were substituted by selenomethionine. However, only three of the four sele-

nomethionine residues were visible in the electron-density map owing to disorder in the region of the N-terminal selenomethionine residue.

*Pf*Rab6t diffraction data for the structure determination were collected to 2.2 Å resolution. The 2.3 Å resolution electron-density map calculated with experimental MAD phases was easily interpretable (Fig. 1). Data in the resolution range 10–2.3 Å were used for refinement; the final $R$ factor for these data was 21.4% and the free $R$ factor was 24.6% (Table 1). The solvent content of the crystal was calculated to be 68% and the Matthews coefficient (Matthews, 1968) was 3.7 Å$^3$ Da$^{-1}$.

The final *Pf*Rab6t model contained residues 11–172, one GDP molecule, one Mg$^{2+}$ ion and 63 water molecules. The geometry for the final model was excellent, with 92% of the protein residues in the core area of the Ramachandran plot and the remaining 8% in the most favorable area. Electron density was missing for Gln41 and was very weak for Asp56 and Glu57. The average overall temperature factor for the crystal structure was 34.3 Å$^2$.

## 4. Discussion

### 4.1. *Pf*Rab6 core structure and consensus elements

The core topology that *Pf*Rab6 shares with other GTPases is characterized by five $\alpha$-helices surrounding a six-stranded $\beta$-sheet. Within this core structure are the five recognized consensus-sequence elements involved in binding an Mg$^{2+}$ ion and either GDP or GTP (Kjeldgaard *et al.*, 1996; Sprang, 1997). Fig. 2 shows the sequence alignment of *Pf*Rab6t with several other GTPases along with the protein structural elements observed for *Pf*Rab6t. The consensus elements are brought together by the core structure to surround and interact with the GDP/GTP molecules and Mg$^{2+}$ ion, as shown in Fig. 3.

The Mg$^{2+}$ ion is located in a deep open pocket (Fig. 4) created by loops $\lambda1$ and $\lambda2$ and helix $\alpha1$. It is coordinated as an octahedral complex involving four water molecules, the Thr25 side-chain hydroxyl group and the $\beta$-phosphate O atom of the GDP. Three of the consensus-sequence elements maintain nearly identical structures independent of hydrolysis and contribute important binding and recognition interactions with the GDP and Mg$^{2+}$ ion. The G*xxxx*GKT/S (P-loop) consensus motif (Saraste *et al.*, 1990) is contained in the first loop $\lambda1$ as residues GEQAVGKT (18–25). Residues of this motif make several
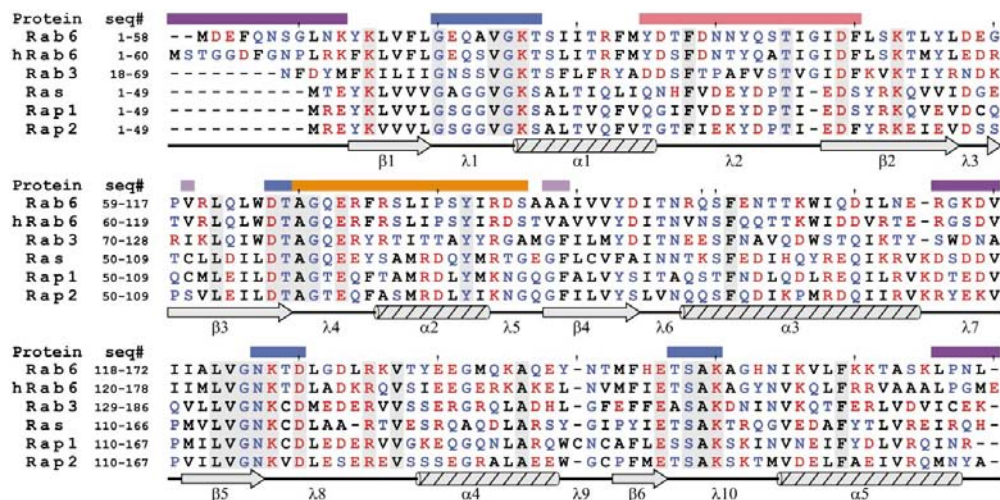


**Figure 2**
Rab6 sequence alignment. The sequence of Rab6t is shown with selected related GTPase sequences, which have been truncated at the end of Rab6t. The amino-acid codes are colored black if hydrophobic, blue if polar and red if charged. A secondary-structure cartoon gives the names assigned to each loop, helix and sheet. Consensus sequences are boxed and colored pink/orange for the switch regions, blue for GDP binding, purple for the CDRs and lavender for the extended CDRs.

hydrogen bonds to phosphate O atoms of the GDP. The Thr25 side-chain hydroxyl group plays a critical role here by providing a hydrogen bond to the $\beta$-phosphate and coordinating the $Mg^{2+}$ ion. It is interesting that the Gln20 side chain appears to block access to the active site by the side chain of Gln70, even though the latter is considered to be critical for stab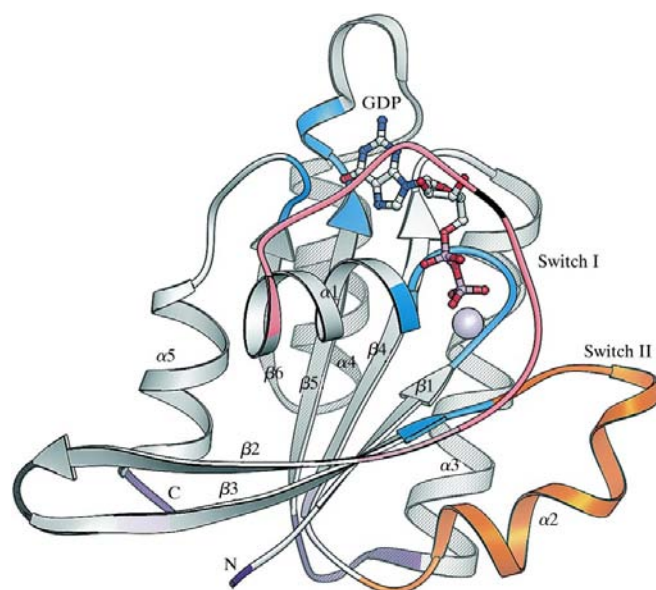ilizing the transition state during hydrolysis (Schweins *et al.*, 1995). This residue corresponds to a much smaller Gly in Ras and Ser in Rab3a (see Fig. 2). The NK*x*D consensus motif is contained in loop $\lambda8$ as residues NKTD (124–127). These residues contribute hydrophobic interactions and hydrogen bonding to the guanine. The hydrogen bonding of the Asp127 side chain to the guanine N1 atom and 2-$NH_2$ atoms appears to be the recognition mechanism that discriminates for the guanine base. The (T/G)(C/S)A consensus motif forms part of loop $\lambda10$ as residues TSA (153–155). These residues also provide hydrogen bonding and hydrophobic interactions with the guanine.

The remaining two consensus-sequence elements are contained in the switch regions. The D*xx*G motif is at the N-terminal end of the switch II region on loop $\lambda4$ and is made up of residues DTAG (66–69). The conserved Asp66 makes an important hydrogen bond to a water molecule that coordinates the $Mg^{2+}$ ion. Gly69 allows conformational flexibility to switch II. The final consensus element is the highly conserved Thr43 located in switch I. The corresponding residue in Ras is Thr35. This switch region undergoes considerable conformational change between the GDP- and GTP-bound states in Ras (Pai *et al.*, 1989, 1990; Brünger *et al.*, 1990) owing to local main-chain $\varphi/\psi$ changes. These cause the conserved Thr residue to roll over upon GTP binding so the side chain points in towards the active site and the hydroxyl group can form a hydrogen bond with the $\gamma$-phosphate O atom. As in Ras–GDP (De Vos *et al.*, 1988), Thr43 in *Pf*Rab6t is flipped the other way so that its side chain points away from the active site. Electron density for the four residues preceding Thr43 is relatively weak and the temperature factors for these residues are high, indicating a region of high mobility and low conformational stability in the GDP-bound state.



**Figure 3**
Ribbon drawing highlighting consensus sequences. The consensus-sequence regions are color-coded as in Fig. 2. Residues not observed in the electron density are shown in black.
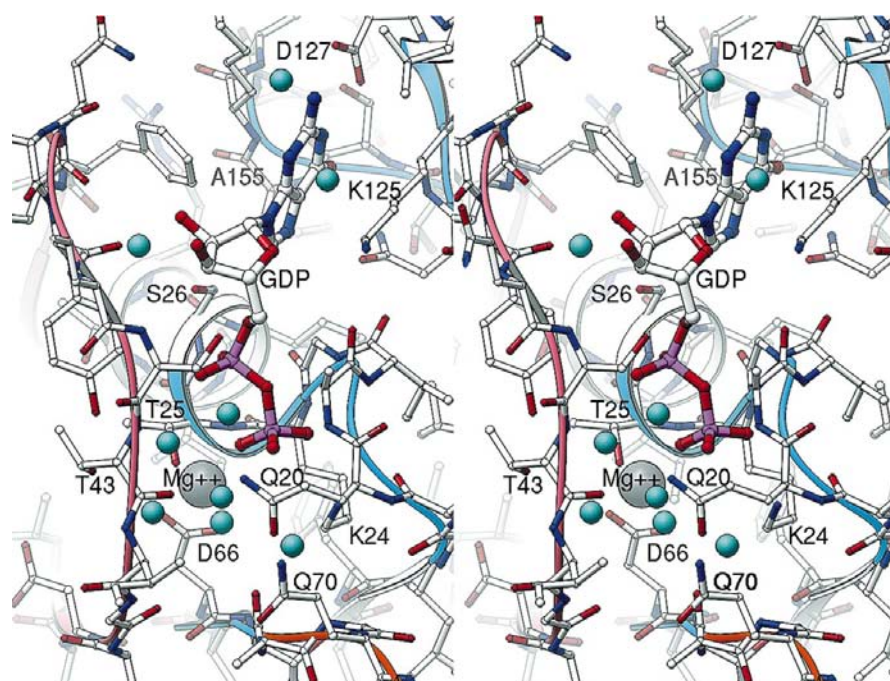
### 4.2. The switch mechanism of Rabs

The switch regions assume different conformations or positions with respect to the molecular framework dependent on whether GDP or GTP is bound. The switch hypothesis suggests that structural changes at the two switch regions occurring in response to nucleotide binding are presented as surface signals to influence effector binding (Kjeldgaard *et al.*, 1996; Sprang, 1997). The switch regions for Rab GTPases were determined for the *Pf*Rab6t structure by comparing it with the two known Rab3A structures. One of these structures contains Rab3A with a GTP analog (Dumas *et al.*, 1999; PDB code 3rab) and the other structure contains GTP-bound Rab3A in complex with the effector domain of Rabphillin-3A (Ostermeier & Brunger, 1999; PDB code 1zbd). Superposition of these molecules showed a very good match for most of the $C^\alpha$ atoms of the core structure, as



**Figure 4**
The GDP/$Mg^{2+}$ binding site in Rab6t. The active site is shown as a ball-and-stick model colored by atom type overlaid on the ribbon drawing colored as in Fig. 3. Water molecules are shown as larger cyan spheres. Key residues are labeled.

well as the GTP/GDP molecules and $Mg^{2+}$ ions (Fig. 5).

Fig. 6 plots differences between the structures of *Pf*Rab6t and the GTP-bound Rab3s along the primary sequence. The lower panel is the distance between corresponding $C^\alpha$ positions, indicative of a translation shift. The middle panel is the difference between corresponding backbone dihedral angles. Large values denote a flip of the peptide plane or a large rotation of a side chain. The upper panel gives the crystallographic temperature factors (*B* factors), indicating mobility and flexibility. Four regions show significant differences in $C^\alpha$ shift or dihedral difference: 33–46, 55–61, 69–83 and 111–116. This provides structural evidence supporting the switch hypothesis in Rab proteins (Kjeldgaard *et al.*, 1996; Sprang, 1997). However, we cannot exclude that some of the observed differences may also represent variations among different subtypes of Rabs.

Comparison of the relative temperature factors (Fig. 6) shows that the GDP-bound form of *Pf*Rab6t demonstrates a higher conformational mobility for the switch I regions than occurs in the Rab3A GTP-bound structures, as expected for Ras-related GTPases. Even so, we were able to see convincing electron density for all main-chain atoms of the switch regions except Gln41. Electron density was also weak for residues 56 and 57. Based on the structural differences between *Pf*Rab6t and Rab3A (Fig. 6), the switch I region is defined as residues 33–47 located in the loop λ2 between helix α1 and strand β2. The *Pf*Rab6t switch II region is defined as residues 68–83 which belong to loop λ4, helix α2 and loop λ5.

Alignment of the *Pf*Rab6t structure with the Rab3A structures suggests the major change in the switch I region upon hydrolysis is a translational shift of those residues along the main chain toward the N-terminus. The maximum shift of over 5 Å is found at residue Thr43. The shift of residues is accompanied by a number of conformational changes along the main chain that relaxes an outward bulge occurring at residues Gly56 and Ile57 in the Rab3As but missing at the corresponding Gly45 and Ile46 in *Pf*Rab6t. The structural alterations result from the changing pattern of coordination to the $Mg^{2+}$ ion and hydrogen bonds to the β- and γ-phosphoryl groups. Switch I also experiences significant $\varphi/\psi$ conformational changes, resulting in a change in the surface residues being presented for effector binding.

Switch II experiences very little $\varphi/\psi$ conformational change, but large alterations in $C^\alpha$ positions. As in other GTPases, the effect of GTP hydrolysis is to change the position and orientation of helix α2. Helix α2 rotates about its axis and shifts as a unit. Three-dimensional alignment of *Pf*Rab6t with Rab3A structures shows a 40° angle between the helices; the center moves about 3 Å. It is noteworthy that in contrast to the Ras–GDP structure (De Vos *et al.*, 1988), this region is well defined in *Pf*Rab6t. The coil-to-helix transition for the N-terminal side of the α2 helix observed for GTP hydrolysis in Ras proteins (Sprang, 1997) was not apparent when comparing *Pf*Rab6–GDP with Rab3A–GTP. The N-terminus of the helix tips slightly outward from the nucleotide-binding site, making it more open. It has been shown that for some mammalian Rabs the GDP-bound state is preferred for binding by GEF (Goud *et al.*, 1990). This slightly more open nucleotide-binding site is likely to facilitate guanine nucleotide exchange.

The generation of different surfaces at the switches provides a mechanistic explanation for Rab–effector interaction. A model of *Pf*Rab6t in the GTP-bound state was constructed based on the *Pf*Rab6t–GDP structure, but with the coordinates from the switch regions generated by homology modeling methods (Sali & Blundell, 1993) using 3rab and 1zbd as templates. Fig. 7 illustrates the different surfaces for effector binding, dependent on whether GTP or GDP is bound.

### 4.3. Effector binding

The crystal structures of a number of Ras-like GTPases bound to effector partners have been reported (Huang *et al.*, 1998; Tesmer *et al.*, 1997; Scheffzek *et al.*, 1997; Rittinger *et al.*, 1997), including the Rab3A complex with Rabphilin-3A (Ostermeier & Brunger, 1999). The common structural theme that arises from these structures is the consistent involvement of the switch I and switch II regions in effector-molecule binding. The Rab3A–Rabphillin structure showed that aside from switch areas, RabCDRs contribute important effector interactions.

The RabCDR of Rab3A is created by the juxtaposition of the N-terminal end of strand β1, the λ7 loop between α3 and β5 and the C-terminus residues. Rab3A and Rab3C have almost identical RabCDRs
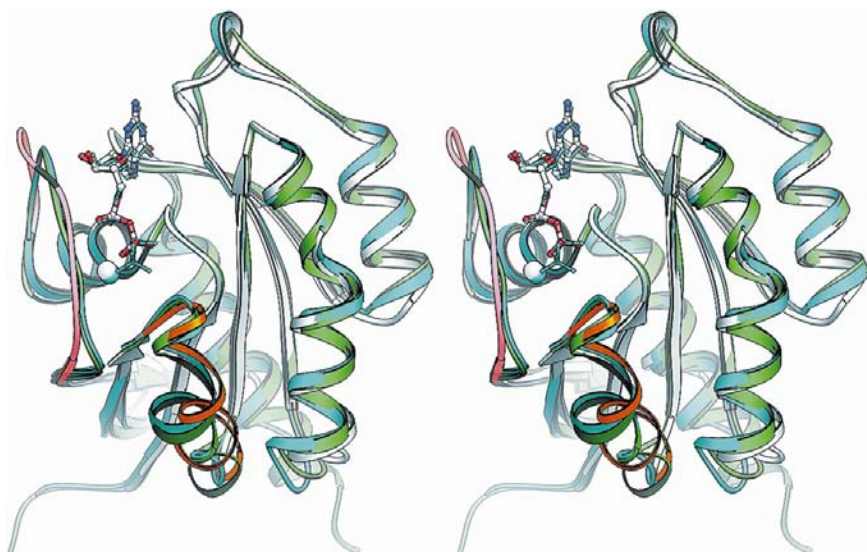


**Figure 5**
Superposition of Rab6t–GDP and Rab3a–GTP. Ribbon drawings of Rab6t with the Rab3s superposed. The Rab6t ribbon is white, with switch regions pink or orange as in Fig. 3. The 3rab ribbon is cyan and the 1zbd ribbon is green. The Rab6t–GDP atoms are shown as a ball-and-stick model colored by atom type. The 3rab nucleotide atoms are shown as smaller balls and sticks colored cyan.
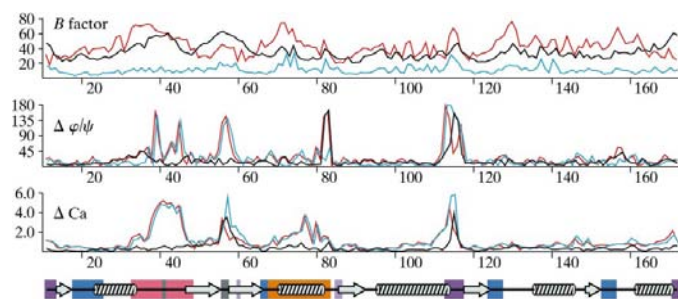
**Figure 6**
Differences between Rab6t–GDP and Rab3–GTP. Comparisons are for the sequence of Rab6t observed in the electron-density map. The upper panel gives the temperature factors (crystallographic *B* factors) for Rab6t (black), 3rab (cyan) and 1zbd (red). The middle panel gives the dihedral differences between the structure for Rab6t *versus* 3rab (cyan), Rab6t *versus* 1zbd (red) and 3rab *versus* 1zbd (black). The dihedral difference was defined as $(\Delta\varphi^2 + \Delta\psi^2)^{1/2}$, where $\varphi$ and $\psi$ are the standard backbone conformation angles. The secondary-structure cartoon and consensus-sequence elements are shown as in Fig. 2. The mean dihedral difference between Rab6t and the Rab3s is 17°; the standard deviation is 24°. The lower panel gives the distance between corresponding CA positions for Rab6t *versus* 3rab (cyan), Rab6t *versus* 1zbd (red) and 3rab *versus* 1zbd (black). The mean distance between Rab6t and the Rab3s is 0.42 Å; the standard deviation is 0.51 Å.
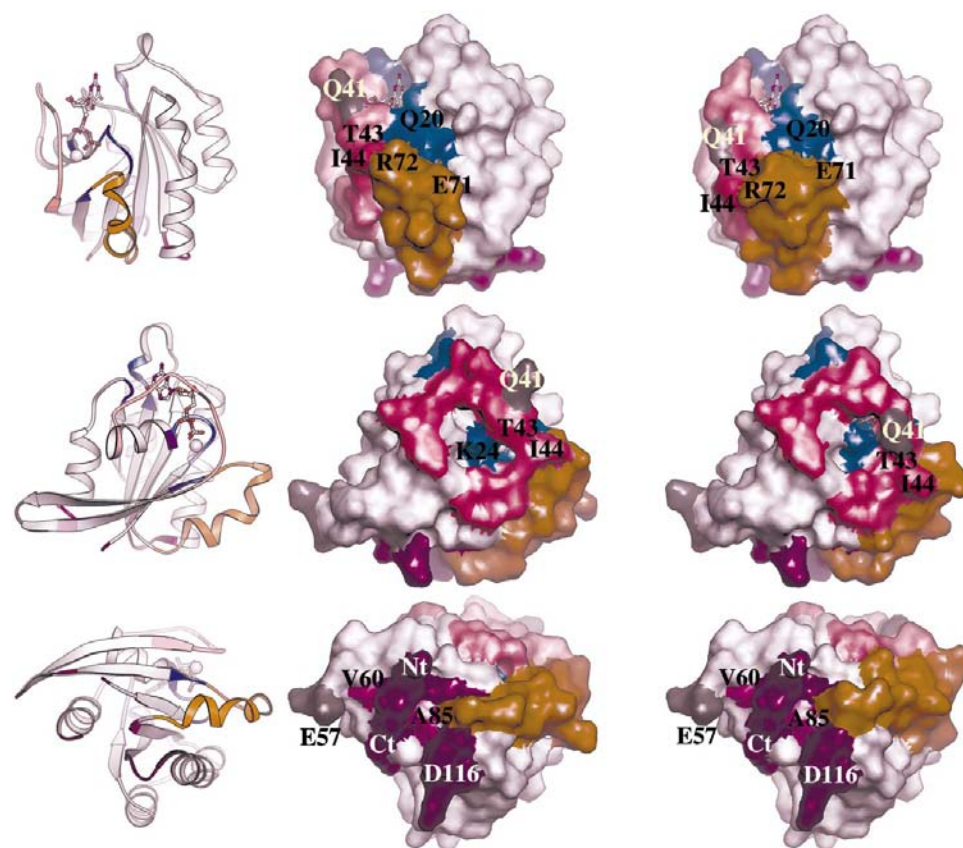


**Figure 7**
Rab6t conformational changes. Three orthogonal views of Rab6t are presented. The coloring of sequence elements is the same as in the other figures. The ribbons and the middle column surfaces are from the GDP-bound Rab6t crystal structure. The surfaces in the right column are from the Rab6–GTP model, as explained in the text. Key residues are labeled. There is essentially no change in the positions of the labeled residues in the bottom row.

and form complexes with Rabphilin-3A; however, other Rab proteins with different RabCDR sequences do not bind Rabphilin-3A (Ostermeier & Brunger, 1999). Amino-acid variability is high for the λ7 loop among the various GTPases, implying that effector-binding signature residues have inter-family sequence variability.

Two different isoforms of human Rab6 have been identified, *viz*. Rab6A and Rab6C, which differ in only three residues (Fitzgerald & Reed, 1999). The Rab6C isoform does not interact with the Rab6A effector Rabkinesin-6, whereas the Rab6A form does (Goud, 1999). The differences between these two isoforms are Val/Ile at position 62 and Thr–Val/Ala–Ala at positions 87–88 (human Rab6 numbering).

In the crystal structure of *Pf*Rab6t, which is an AA variant (*i.e.* equivalent to Rab6C), the residues corresponding to the isoform residues of human Rab6 are Val60, Ala85 and Ala86. Val60 is partially exposed and involved in a hydrophobic interaction with residues at the N-terminus just after the N-terminal CDR, which are unobserved owing to disorder in the GDP-bound structure. The conservative substitution of Ile for the Val at residue 60 probably would not significantly alter the packing environment of the surrounding residues, whereas less conservative substitutions might alter the positions of nearby RabCDR residues of the N-terminus.

In *Pf*Rab6t, Ala85 is well exposed while Ala86 is totally buried, which suggests that amino acids at position 85 are crucial for intermolecular interactions with Rab6 effectors. In addition, Ala86 mutations might also have an effect on local packing that could impact on external Ala85 interactions. These isoform-specific amino acids, along with the N-terminal residues, C-terminal residues and RabCDR (113–117), make a cluster on the surface of the *Pf*Rab6t molecule situated on the opposite side of the molecule from the GDP/GTP-binding site (Fig. 7). The entire cluster forms a surface patch approximately 15 Å wide and 30 Å long. The newly identified isoform residues appear to constitute an expansion of the RabCDR domain.

It is striking that both *P. falciparum* and *S. cerevisiae* which have simple Golgi structures also have unique *rab6* genes encoding the AA-like (Rab6C) motif. This suggests that the acquisition of the Rab6A (TV) isoform was coincident with the development of a more complex Golgi structure and

perhaps the necessity of performing retrograde transport from the distal cisternae to the ER. As only Rab6A and not Rab6C binds to Rabkinesin-6, it follows that neither *Pf*Rab6 (nor *YPT6*, the yeast homolog of Rab6) would interact with the lower eukaryote parasite equivalent of Rabkinesin-6. Interestingly, a Rabkinesin-6 homologue has not been identified in either the *P. falciparum* or *S. cerevisiae* genomes. This argues that *Pf*Rab6 might not require binding to a Rabkinesin-6-like effector (or any motor-like effector) to assure its function within the parasite's rudimentary Golgi organelle. Instead, it is possible that *Pf*Rab6 (and YPT6) derives force and direction of trafficking by binding another type of motor, such as some other kinesin-like molecule or actinomyosin (Pinder *et al.*, 1998).

Rab GTPases are at the middle of a complex web of molecular interactions which accomplish the necessary sorting and transport of cellular proteins and materials *via* vesicle transport. However, it is possible and perhaps likely that there are still other yet unidentified portions of Rab molecules important for intermolecular interactions.

## References

Antony, C., Cibert, C., Geraud, G., Santa Maria, A., Maro, B., Mayau, V. & Goud, B. (1992). *J. Cell Sci.* **103**, 785–796.

Brunger, A. T., Adams, P. D., Clore, G. M., DeLano, W. L., Gros, P., Grosse-Kunstleve, R. W., Jiang, J.-S., Kuszewski, J., Nilges, M., Pannu, N. S., Read, R. J., Rice, L. M., Simonson, T. & Warren, G. L. (1998). *Acta Cryst.* D**54**, 905–921.

Brünger, A. T., Milburn, M. V., Tong, L., de Vos, A. M., Jancarik, J., Yamaizumi, Z., Nishimura, S., Ohtsuka, E. & Kim, S.-H. (1990). *Proc. Natl Acad. Sci. USA*, **87**, 4849–4853.

Carson, M. (1997). *Methods Enzymol.* **277**, 493–505.

Castro, F. A. de, Ward, G. E., Jambou, R., Attal, G., Mayau, V., Jaureguiberry, G., Braun-Breton, C., Chakrabarti, D. & Langsley, G. (1996). *Mol. Biochem. Parisitol.* **80**, 77–88.

Chattopadhyay, D., Smith, C. D., Barchue, J. & Langsley, G. (2000). *Acta Cryst.* D**56**, 1017–1019.

Collaborative Computational Project, Number 4 (1994). *Acta Cryst.* D**50**, 760–763.

De Vos, A. M., Tong, L., Milburn, M. V., Matias, P. M., Jancarik, J., Noguchi, S., Nishimura, S., Miura, K., Ohtsuka, E. & Kim, S.-H. (1988). *Science*, **239**, 888–893.

Dumas, J. J., Zhu, Z., Connolly, J. L. & Lambright, D. G. (1999). *Structure*, **7**, 413–422.

Echard, A., Jollivet, F., Martinez, O., Lacapere, J. J., Rousselet, A., Janoueix-Lerosey, I. & Goud, B. (1998). *Science*, **279**, 580–585.

Fitzgerald, M. L. & Reed, G. L. (1999). *Biochem. J.* **342**, 353–360.

Girod, A., Storrie, B., Simpson, J. C., Johannes, L., Goud, B., Roberts, L. M., Lord, J. M., Nilsson, T. & Pepperkok, R. (1999). *Nature Cell. Biol.* **1**, 423–430.

Goud, B. (1999). Personal communication.

Goud, B., Zahraoui, A., Tavitian, A. & Saraste, J. (1990). *Nature (London)*, **345**, 553–556.

Huang, L., Hofer, F., Martin, G. S. & Kim, S.-H. (1998). *Nature Struct. Biol.* **5**, 422–426.

Kjeldgaard, M., Nyborg, J. & Clark, B. F. C. (1996). *FASEB J.* **10**, 1347–1368.

Lu, G. (1996). *Protein Data Bank Quart. Newslett.* **78**, 10–11.

Martinez, O. & Goud, B. (1998). *Biochim. Biophys. Acta*, **1404**, 101–112.

Matthews, B. W. (1968). *J. Mol. Biol.* **33**, 491–497.

Nuoffer, C. & Balch, W. E. (1994). *Annu. Rev. Biochem.* **63**, 949–990.

Ostermeier, C. & Brunger, A. T. (1999). *Cell*, **96**, 363–374.

Pai, E. F., Kabsch, W., Krengel, U., Holmes, K. C., John, J. & Wittinghofer, A. (1989). *Nature (London)*, **341**, 209–214.

Pai, E. F., Krengel, U., Petsko, G. A., Goody, R. S., Kabsch, W. & Wittinghofer, A. (1990). *EMBO J.* **9**, 2351–2359.

Pfeffer, S. R. (1994). *Curr. Opin. Cell Biol.* **6**, 522–526.

Pflugrath, J. W. (1999). *Acta Cryst.* D**55**, 1718–1725.

Pinder, J. C., Fowler, R. E., Dluzewski, A. R., Bannister, L. H., Lavin, F. M., Mitchell, G. H., Wilson, R. J. & Gratzer, W. B. (1998). *J. Cell Sci.* **111**, 1831–1839.

Rittinger, K., Walker, P. A., Eccleston, J. F., Smerdon, S. J. & Gamblin, S. J. (1997). *Nature (London)*, **389**, 758–762.

Sali, A. & Blundell, T. L. (1993). *J. Mol. Biol.* **234**, 779–815.

Saraste, M., Sibbald, P. R. & Wittinghofer, A. (1990). *Trends Biochem. Sci.* **15**, 430–434.

Scheffzek, K., Ahmadian, M. R., Kabsch, W., Weismüller, L., Lautwein, A., Schmitz, F. & Wittinghofer, A. (1997). *Science*, **277**, 333–338.

Schimmöller, F., Simon, I. & Pfeffer, S. R. (1998). *J. Biol. Chem.* **273**, 22161–22164.

Schweins, T., Geyer, M., Scheffzek, K., Warshel, A., Kalbitzer, H. R. & Wittinghofer, A. (1995). *Nature Struct. Biol.* **2**, 36–44.

Sprang, S. (1997). *Annu. Rev. Biochem.* **66**, 639–678.

Strom, M., Vollmer, P., Tan, T. J. & Gallwitz, D. (1993). *Nature (London)*, **361**, 736–739.

Templeton, T. J. & Kaslow, D. C. (1998). *Mol. Biochem. Parasitol.* **94**, 149–153.

Terwilliger, T. C. & Berendzen, J. (1999). *Acta Cryst.* D**55**, 849–861.

Tesmer, J. J., Sunahara, R. K., Gilman, A. G. & Sprang, S. R. (1997). *Science*, **278**, 1898–1899.

Ward, G. E., Tinley, L. G. & Langsley, G. (1997). *Parasitol. Today*, **13**, 57–62.